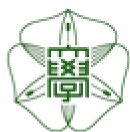

HOKKAIDO UNIVERSITY

Title	X-ray photoelectron spectroscopy study on effects of ultra-high-pressure annealing on surface of Mg-ion-implanted GaN
Author(s)	Akazawa, Masamichi; Wu, Encheng; Sakurai, Hideki; Bockowski, Michal; Narita, Tetsuo; Kachi, Tetsu
Citation	Japanese Journal of Applied Physics (JJAP), 60(3), 036503 https://doi.org/10.35848/1347-4065/abe609
Issue Date	2021-03-01
Doc URL	http://hdl.handle.net/2115/84214
Rights	©2021 The Japan Society of Applied Physics
Rights(URL)	https://creativecommons.org/licenses/by-nc-nd/4.0/
Type	article (author version)
File Information	JJAP_RP_Akazawa_XPSUHPA_ver10.pdf

Instructions for use

Hokkaido University Collection of Scholarly and Academic Papers : HUSCAP

X-ray photoelectron spectroscopy study on effects of ultra-high-pressure annealing on surface of Mg-ion-implanted GaN

Masamichi Akazawa[1,*], Encheng Wu[1], Hideki Sakurai[2,3,4], Michal Bockowski[3,5], Tetsuo Narita[6] and Tetsu Kachi[3]

[1]*Research Center for Integrated Quantum Electronics, Hokkaido University, Sapporo, Hokkaido 060-0813, Japan*

[2]*Department of Electronics, Graduate School of Engineering, Nagoya University, Nagoya, Aichi 464-8601, Japan*

[3]*Institute of Materials and Systems for Sustainability, Nagoya University, Nagoya, Aichi 464-8601, Japan*

[4]*Institute for Semiconductor & Electronics Technology, ULVAC, Inc., Chigasaki, Kanagawa 253-8543, Japan*

[5]*Institute of High Pressure Physics, Polish Academy of Sciences, Sokolowska 29/37, 01-142 Warsaw, Poland*

[6]*Toyota Central R&D Labs., Inc., Nagakute, Aichi 480-1192, Japan*

*E-mail: akazawa@rciqe.hokudai.ac.jp

The effects of ultra-high-pressure annealing (UHPA) on the surface of Mg-ion-implanted GaN were investigated by X-ray photoelectron spectroscopy (XPS). After Mg ion implantation or Mg–N co-implantation, GaN was annealed at 1400 °C for 5 min under a nitrogen pressure of 1 GPa. No deterioration of the surface stoichiometry occurred after UHPA despite the extremely high annealing temperature. The angle-resolved XPS with calibration showed that the surface Fermi level was pinned at 0.5 eV from the conduction band edge after dehydrogenation subsequent to UHPA. However, the absence of pinning at the charge neutrality level showed that surface disorder was absent after UHPA. The surface photovoltaic effect as an evidence of the achievement of p-type conduction even in the near–surface region was more remarkable for Mg–N-ion-implanted samples after dehydrogenation subsequent to UHPA. There is a possibility that the density of N-vacancy-related defects was reduced more by Mg–N co-implantation.

1. Introduction

GaN has a wide band gap, a high breakdown field, a high electron mobility, a high saturation electron velocity, and good thermal conductivity[1–3]. Compared with other wide-band-gap semiconductors, *e.g.*, SiC and diamond, which are also promising materials for power device applications, GaN has the advantage that it can be combined with other III-nitride alloys, such as AlGaN, InAlN, and InAlGaN, to provide an excellent heterointerface while generating a two-dimensional electron gas with a high electron mobility. Furthermore, an excellent MOS structure with an extremely minimized interface state density at the insulator/GaN interface can be obtained [4–6]. Even an excellent MOS gate high-electron-mobility transistor can also be achieved[7]. This is surprising because the interface between an insulator and III-V compound semiconductors is usually characterized by a high density of interface states. Owing to these features, recently, this material has attracted much attention with the expectation of realizing a high-efficiency power device for decreasing electrical energy consumption[8, 9]. In particular, the vertical MOS field-effect transistor (MOSFET) attracts much attention[10–12].

Power devices usually require selectively doped parts, including a guard ring and a junction thermal extension, to enhance their performance and achieve a high efficiency. Ion implantation is a useful technique for selective doping in the fabrication of power devices. However, it is generally difficult to obtain p-type GaN by ion implantation. Although Mg ion implantation (Mg-I/I) is considered to be the most promising method, p-type conduction in GaN had not been achieved. However, recently, p-type conduction in Mg-ion-implanted GaN has been successfully achieved[13–21]. The key to this achievement was increasing the temperature during annealing. It was reported that the temperature should be 1230 °C or higher to obtain p-type conduction with Mg-ion-implanted GaN by conventional rapid thermal annealing (RTA) with atmospheric-pressure nitrogen flow[17–20]. On the other hand, symmetric multicycle RTA in which the temperature was increased in sequential pulses from 1000 to 1420 °C under a nitrogen pressure of 2 MPA has been reported to achieve a high activation ratio of up to 10% without surface degradation[13–16]. More recently, it has been reported that ultra-high-pressure annealing (UHPA), in which the temperature was increased to 1400 °C under a nitrogen pressure of 1 GPa for Mg-ion-implanted GaN, achieved a p-type conduction that was completely confirmed by Hall effect measurement[21]. In the same study, the activation energy of Mg acceptors was measured to be 212 meV, whereas the Hall mobility of holes was 24.1 $cm^{-2}V^{-1}s^{-1}$ at 300 K for UHP-annealed Mg-ion-implanted GaN with an acceptor concentration of 2.6×10^{18} cm^{-3}.

It was also concluded that more than 70 % of the implanted Mg atoms were activated as acceptors through UHPA. Nevertheless, the effects of UHPA on the surface of Mg-ion-implanted GaN have not yet been investigated in detail, even though atomic force microscopy (AFM) revealed that no surface roughness degradation occurred after UHPA[21].

In the application of GaN to power devices, the control of the surface and interfaces is an important problem. In particular, the insulator/semiconductor interface should be controlled to realize a MOSFET with a high performance. To control such an interface, we should start by investigating the surface of UHP-annealed Mg-ion-implanted GaN. X-ray photoelectron spectroscopy (XPS) is a powerful technique for investigating a semiconductor surface. By XPS, we can investigate not only the chemical composition of the surface but also surface band bending. Substantially, the angle-resolved XPS (ARXPS) technique enables us to investigate abrupt surface band bending[22–24]. For p-type GaN, however, it has been reported that the surface photovoltage (SPV) effect[25], where the band bending is reduced by the transfer of electrons and holes generated by X-ray illumination, is significant even at room temperature[26]. Nevertheless, the observation of this phenomenon may lead to the confirmation of the p-type conduction in the near-surface region of a semiconductor. The Fermi level pinning position may be derived by calibrating the binding energy.

Here, we investigated the effects of UHPA on the surface of Mg-ion-implanted GaN by XPS. We also investigated Mg–N-ion-co-implanted GaN. The stoichiometry, SPV effect, band bending, and Fermi level pinning position at the surface of the implanted GaN after UHPA were examined by XPS.

2. Experimental procedure

The sample preparation sequence and sample structure are shown in Figs. 1(a) and (b), respectively. First, a 2-μm-thick undoped GaN layer was grown on a free-standing substrate via a 0.2-μm-thick n^+-GaN buffer layer by metalorganic vapor phase epitaxy. Thereafter, Mg-I/I was carried out at room temperature. For comparison, a sample with Mg–N-ion-co-implantation (Mg–N-I/I) was also prepared with the same maximum concentrations of implanted Mg and N. Then, UHPA was performed under a nitrogen pressure of 1 GPa at 1400 °C for 5 min. The resultant Mg concentration [Mg] measured by secondary ion mass spectroscopy (SIMS) was $2–3\times10^{18}$ cm^{-3} from the surface to a depth of ~500 nm, as shown in Fig. 2(a), where the hydrogen density [H] profile is also plotted. H

atoms might have come from the moisture in the UHPA system because of the difficulty of complete purge[27]. The [H] profile is very similar to the [Mg] profile, which may indicate the possibility of Mg passivation by H. This similar situation can be seen for the sample with Mg–N-I/I as shown in Fig. 2(b). Therefore, additional annealing for the dehydrogenation of Mg dopants was carried out at 850 °C for 60 min under atmospheric nitrogen flow in an ordinary furnace. A sufficient decrease in [H] induced by this annealing condition was confirmed by a separate experiment. After UHPA, sulfuric peroxide mix (SPM) surface treatment, at a temperature below 80 °C, followed by buffered hydrofluoric acid (BHF) treatment was carried out. After dehydrogenation annealing, BHF treatment was carried out. XPS was performed at each step of the sample preparation sequence using a monochromated Al-$K\alpha$ X-ray source (1486.6 eV).

We confirmed that the surface of GaN was not etched by SPM treatment. After partial etching by covering one side of the GaN chip with Al_2O_3, AFM was performed to detect an etch step formed by 10-times-repeated SPM treatment. However, we did not find any boundaries. In addition, the surface morphology was not affected by SPM treatment. As shown in Fig. 3, the AFM image of the GaN surface after 1-time SPM treatment (Fig. 3(b)) and even after 10-times-repeated SPM treatment (Fig. 3(c)) did not show any differences compared with that of the GaN surface without SPM treatment (Fig. 3(a)), indicating that their root mean square (RMS) roughnesses are similar. It is highly likely that the sample surface was not etched by SPM treatment because the treatment temperature was sufficiently low. Therefore, the sample surface was cleaned by this treatment without losing information about the effect of UHPA.

3. Results and discussion

3.1 Surface stoichiometry at each process step

The surface stoichiometry might be changed by UHPA because the temperature was as high as 1400 °C even under the nitrogen pressure of 1 GPa. Therefore, the surface stoichiometry should be examined. In particular, the absence of nitrogen desorption from the GaN surface should be confirmed, even though the nitrogen pressure of 1 GPa is sufficiently higher than the nitrogen equilibrium partial pressure[21, 28]. Figures 4 (a) to (d) show N 1s spectra with Ga LMM Auger spectra and Ga 3d spectra with N 2s spectra, for each step of the sample preparation process. Here, the photoelectron take-off angle θ was set at 45°. A Ga LMM Auger spectrum was decomposed into three components according to the literature[29, 30], whereas a Ga 3d spectrum was fitted by the combined Voigt function considering the

spin-orbit doublet. The intensity was normalized to the area of the Ga 3d spectrum. Although the height of the N 1s N–Ga bonding component peak was reduced after Mg-I/I and the subsequent process steps, the area of this spectrum remained almost the same. Therefore, no evidence of nitrogen deficiency at the sample surface was observed. Although the increase in peak width for Mg-I/I and subsequent process steps may have been caused by band bending[22, 24], a detailed analysis is beyond the scope of this study. (Band bending in the as-implanted GaN might have been generated by acceptor-like defects.) More specifically, the ratio of the spectral area of the N 1s spectrum, I_{N1s}, to that of the Ga 3d spectrum, I_{Ga3d}, for GaN at each process step is plotted in Fig. 5. Here, the component A shown in Fig. 4 (b) for the as-implanted GaN is excluded in the calculation of the N 1s area because it should be assigned to the N–O bonding of the surface oxide[29, 30], although the reason why this component was remarkable at the Mg-I/I step is unclear. If nitrogen deficiency occurred, these ratios should become lower than those of the as-grown GaN. However, the I_{N1s}/I_{Ga3d} ratio remained almost the same as that of the as-grown GaN after Mg-I/I, UHPA, and dehydrogenation. Therefore, the surface stoichiometry was maintained without nitrogen desorption even after 1400 °C/5 min annealing. This result shows the efficiency of applying an ultra-high nitrogen pressure during annealing at a temperature as high as 1400 °C.

3.2 SPV as evidence of p-type conductivity

SPV that reduces band bending is reported to be significant in the XPS of p-type GaN even at room temperature[26]. Figure 6 shows the schematic of the SPV effect. The electron–hole pairs generated in the depletion layer by X-ray illumination should be separated by a strong internal field owing to surface band bending. Thereafter, the holes move deeper inside, while the electrons move to the surface. Consequently, band bending under illumination should be reduced compared with that in the dark. Obviously, the core level related to the constituent elements in GaN also moves. Therefore, the SPV effect is usually observed as a shift of these core levels by X-ray illumination. Here, let us focus on the behavior of the core-level spectrum from the absorbed carbon atoms, *i.e.*, the C 1s spectrum. This spectrum is often used to calibrate the charge up due to the loss of electrons at the sample surface, especially for a high-resistivity material. In this case, the C 1s spectrum should shift to a higher binding energy. However, if SPV dominates in p-GaN, the C 1s spectrum should move to a lower binding energy because SPV reduces the binding energy of C 1s, as indicated in Fig. 6.

Actually, the Mg-ion-implanted GaN and Mg–N-ion-implanted GaN after UHPA and

subsequent dehydrogenation annealing showed a C 1s spectral shift to a binding energy lower than the benchmark energy of 285.0 eV[31)], whereas the as-grown sample, as-implanted sample, and the sample after UHPA without dehydrogenation annealing showed opposite shifts. Figure 7 shows the C 1s spectra for all process steps measured at θ = 45° for Mg-ion- and Mg–N-ion-implanted GaN samples. An opposite shift for the final process step can be clearly seen for both implanted samples. The C 1s spectra at the as-grown and Mg-I/I steps showed a positive shift dominated by a charge-up presumably due to the loss of electrons at the surface, while the C 1s spectral shift after dehydrogenation was negative owing to SPV for both the Mg-ion- and M–N-ion-implanted GaN samples. After UHPA, since a positive shift smaller than those at the previous process steps was observed, SPV might have been small. We performed ARXPS at each step of the sample preparation process. The average shift of the C 1s spectrum over five measurements at various θ values for each process step is summarized in Fig. 8. It can be seen that SPV emerged after dehydrogenation subsequent to UHPA for both the Mg- and M–N-implanted GaN samples. It should be noted that SPV was more significant for the M–N-implanted GaN sample. This difference is discussed later. Nevertheless, SPV implied the possibility of downward band bending.

3.3 Confirmation of p-type band bending

When band bending within the photoelectron escape depth is negligible, the Fermi level position E_F relative to the valence band maximum (VBM) E_V can be derived as

$$E_F - E_V = E_F - E_{Ga3d} - (E_V - E_{Ga3d}) = B_{Ga3d} - (B_{Ga3d} - B_{VBM}), \qquad (1)$$

where E_{Ga3d} is the Ga 3d core level energy, and B_{Ga3d} and B_{VBM} are the binding energies of Ga 3d and VBM, respectively. Here, (B_{Ga3d} – B_{VBM}) is a material constant of GaN. Once (B_{Ga3d} – B_{VBM}) is known, (E_F – E_V) can be obtained by measuring B_{Ga3d}. To apply this method to an actual GaN surface, (B_{Ga3d} – B_{VBM}) should be measured. Figure 9 shows Ga 3d and VBM spectra of the as-grown undoped GaN layer measured at θ = 45°. Similar results were obtained at θ = 15°, 30°, 60°, and 90°. B_{VBM} was derived from the extrapolation of the lower-binding-energy edge of the VBM spectra. As the average of all data obtained at five θ values, (B_{Ga3d} – B_{VBM}) = 17.2 eV. With θ, the photoelectron escape depth λ is changed as

$$\lambda = \lambda_0 sin\theta, \qquad (2)$$

where λ_0 is the inelastic mean free path of the photoelectron in GaN. Here, λ_0 was calculated to be 2.57 nm for the Ga 3d spectrum according to the literature[32, 33]. Using this value, we can derive ($E_F - E_V$) at each λ from the Ga 3d spectrum as shown in Fig. 10(a), where the values derived directly from the VBM spectral edge are also shown. An excellent coincidence between the values obtained by both methods, *i.e.*, Ga 3d-based and VBM-based methods, can be seen. Thus, we can derive the ($E_F - E_V$) value from the Ga 3d spectrum. We also confirmed that the spectral shapes coincided between the Ga 3d spectra at $\theta = 15^\circ$ and 90°, which indicated that the effect of the surface oxide on the ($E_F - E_V$) determination could be ignored in the analysis of this spectrum. For the as-implanted sample, ARXPS indicated the E_{FS} located at $E_C - 0.9$ eV as shown in Fig. 10(b). This position coincides with the measured charge neutrality level E_{CNL}[34], which indicated that the structural disorder, or lattice disorder, in the implanted GaN was severe.

ARXPS is a convenient method of distinguishing the existence of abrupt band bending at the surface of a semiconductor[22–24]. As described above, when the depletion layer width is sufficiently larger than the photoelectron escape depth and surface band bending is not abrupt, the measured ($E_F - E_V$) should be unchanged at any θ, as shown in Fig. 10(a). However, when the doping concentration is sufficiently high to result in a small depletion width with abrupt surface band bending, resulting in a large variation in potential within the photoelectron escape depth, ($E_F - E_V$) should be changed by θ or λ. This phenomenon should be reflected in the binding energy of the Ga 3d spectrum. Namely, if abrupt band bending exists at the GaN surface, the Ga 3d spectrum shifts monotonically with θ.

In the implanted sample, the Mg doping concentration was sufficiently high to make the surface band bending abrupt. The expected θ-dependent shifts of the Ga 3d spectrum were observed for the sample after dehydrogenation annealing subsequent to UHPA as shown in Fig. 11. As θ was decreased to make the analysis surface-sensitive, B_{Ga3d} increased. According to Eqs. (1) and (2), this means that ($E_F - E_V$) increased, or E_F approached E_C, as λ or probing depth decreased.

($E_F - E_V$) under X-ray illumination derived from the Ga 3d spectrum is plotted versus θ in Fig. 12(a) for Mg-implanted and Mg–N-implanted samples. This plot shows that the present samples after the completion of the dopant activation exhibited abrupt p-type surface band bending, which indicates the successful achievement of the p-type conduction even in the near-surface region. If ($E_F - E_V$) in the dark can be derived, it is useful information.

3.4 Correction of surface photovoltaic effect

Considering the mechanism shown in Fig. 6, the calibration method based on the C 1s peak position used for the samples without SPV can be applied to the sample after dehydrogenation with SPV. The results with this calibration are shown by the solid circles in Fig. 12(b). Here, the calibration was carried out for each θ using each C 1s shift. (The C 1s shift in Fig. 8 is the average value over all θ values.) In this figure, the solid line is the line fitted on the basis of the simulation results assuming the surface Fermi level pinning at E_C – 0.5 eV. The details of the simulation are described in Ref. 24. Briefly, the XPS peak position is given by the integration of the photoelectron response spectrum at each depth along the bent band. In this simulation, the core-level spectral intensity I as a function of the binding energy E is given by

$$I(E) = \int_0^\infty I_0(E,z) exp\left(-\frac{z}{\lambda}\right) dz, \tag{3}$$

where $I_0(E, z)$ is the intensity of photoelectron response at E and the depth z. $I_0(E, z)$ is given by the Voigt function, which has a peak at E_0. Taking into account band bending, E_0 is a function of z. The relationship between E_0 and z is given by considering the solution of the Poisson equation. The simulation result shown in Fig. 12(b) is in good agreement with the experimental data. Therefore, the surface Fermi level E_{FS} of both samples should have been pinned at E_C – 0.5 eV upon dehydrogenation subsequent to UHPA.

3.5 Origin of E_{FS} pinning

After UHPA and subsequent dehydrogenation, E_{FS} located at E_C – 0.5 eV. Because the band bending was downward, the charge generated by Mg acceptors in the depletion layer was negative. Therefore, positive charge should have existed at the surface or in the near-surface region. This indicated the existence of the donor-like bulk defect level at E_C – 0.5 eV in the near-surface region by the reason as follows. According to the disorder-induced gap state model concerning the origin of semiconductor surface/interface states, the surface states density (N_{SS}) distributes in a U shape in the band gap[35]. The U-shaped N_{SS} distribution has been confirmed experimentally on the GaN bare surface[36]. Figure 13 shows a schematic diagram of the charge-up mechanism of surface states. The surface states on the upper side above E_{CNL} (E_C – E_{CNL} = 0.9 eV[34]) are acceptor-like states, while the surface states located below E_{CNL} are donor-like states[35]. With the E_{FS} position at

E_C – 0.5 eV above E_{CNL}, the surface states should be charged up negatively (Fig. 13(a)). Therefore, positive charges cannot be generated by the surface states unless E_{FS} locates below E_{CNL} (Fig. 13(b)). Thus, the positive surface charge should have been generated by the donor-like bulk defect level in the near-surface region of GaN after UHPA and subsequent dehydrogenation. Consequently, a donor-like defect level at E_C – 0.5 eV should have existed in both samples in addition to surface states.

Combined with the retention of the surface stoichiometry after UHPA, the donor-like defect level at E_C – 0.5 eV was unlikely assigned to the V_N-related defect. On the basis of the previously reported calculation results[37)], no simple defects produce a donor-like defect level at E_C – 0.5 eV. Instead, according to Refs. 38–41, the bulk defect level at E_C – 0.5 eV might be related to the dislocations. Actually, a transmission electron microscopy study showed that interstitial-type extended defects and inversion domains were generated in the GaN bulk after UHPA at 1300 °C, while vacancy-type extended defects were observed after UHPA at 1480 °C.[42)]

3.6 Origin of SPV difference caused by N-co-implantation

It should be noted that E_{FS} was not pinned at E_{CNL}, where pinning occurs with high a density of surface states for both samples in Fig. 12(b). If the surface disorder is severe, a high N_{SS} pins E_{FS} at E_{CNL}. Therefore, the E_{FS} location at E_C – 0.5 eV sufficiently above E_{CNL} indicated the absence of a severe disorder at the surface. Combined with the result that the stoichiometry of the GaN surface did not deteriorate, UHPA never deteriorates the GaN surface.

Despite the same E_{FS} pinning position and band bending in the dark, as shown in Fig. 12(b), SPV was more significant for the Mg–N-implanted GaN, as shown in Figs. 8 and 12(a). There is a possibility that there are less amounts of defects in the Mg–N-ion-implanted sample by the following reason. The photocurrent J_{ph} under X-ray illumination is given by[43)]

$$J_{ph} = q\Phi[1 - \exp(-\alpha W)], \tag{4}$$

where q is the elementary charge, Φ is the incident photon flux density, α is the absorption coefficient, and W is the depletion layer width. In the steady state, J_{ph} should balance with the sum of the restore current and the recombination current J_{rec}. J_{rec} might consist of

surface recombination due to the surface states and bulk recombination due to the defect levels. The restore current should be thermionic-field-emission (TFE) current given by[44)]

$$J_{TFE}(V) = \frac{A^{*}T\sqrt{\pi E_{00} q(\phi_B+\phi_p-V)}}{k \cosh(E_{00}/kT)} exp\left[\frac{q\phi_p}{kT} - \frac{q(\phi_B+\phi_p)}{E_0}\right] exp\left(\frac{qV}{E_0}\right), \quad (5)$$

where

$$E_{00} = \frac{qh}{4\pi}\sqrt{\frac{N_A}{m^{*}\varepsilon_S}}, \quad (6)$$

$$E_0 = E_{00}\coth\left(\frac{E_{00}}{kT}\right), \quad (7)$$

A^* is the Richardson constant, T is the temperature, ϕ_B is the Schottky barrier height, $\phi_p = E_C - E_F$, V is SPV, k is the Boltzmann constant, h is the Plank constant, m^* is the effective mass of a hole, ε_S is the dielectric constant, and N_A is the acceptor concentration. However, we found that J_{TEF} with E_{00} given by Eq. (6) was very small compared with J_{ph}. According to Ref. 45, defects in the near-surface region can increase E_{00} by enhancing the tunneling current, which is considered here. Let us assume that the following equation was achieved by the Mg-ion-implanted sample, *i.e.*,

$$J_{TFE}(0.6\text{ V}) = J_{ph} - J_{rec}, \quad (8)$$

and

$$J_{TFE}(0.8\text{ V}) = J_{ph} - BJ_{rec} \quad (9)$$

was achieved by the N-co-implanted sample for the same J_{ph}, where B is the multiplying factor. Although the estimation of Φ is difficult, it seems to range from 10^{12} to 10^{13} cm^{-2}s^{-1} [25, 45)]. For estimating J_{ph}, we use α = 800 cm^{-1} [46)] and W = 20 nm. If we assume the same value of E_{00} for both samples, we can calculate J_{TFE} for each V. Thereafter, B and J_{rec} can be derived from Eqs. (8) and (9). Figure 14 shows B calculated as a function of E_{00}. B less than unity is calculated for possible E_{00} in the range where J_{TFE} is comparable to J_{ph}. Since the surface states seem to be similar for both samples considering the same Fermi level pinning

position, this estimation result indicated that the defect density in the GaN bulk was reduced by N-co-implantation. Actually, it has been reported that the density of N-vacancy (V_N)-related defects was reduced by N-co-implantation at the as-implanted process step[47]. Although the density of V_N-related defects is reduced by UHPA even for the Mg-ion-implanted sample[21], there is a high possibility that the initial reduction led to a further reduction in the V_N-related defects upon UHPA for the Mg–N-ion-implanted sample. In other words, it is highly likely that the N-co-implantation combined with UHPA is effective for a thorough reduction in the density of V_N-related defects. A $Mg_{Ga}V_N$ complex defect can be a donor to compensate for the Mg acceptor[37]. Therefore, there is a possibility that the acceptor compensation rate was improved by N-co-implantation.

4. Conclusions

The effects of UHPA on the surface of Mg-ion-implanted GaN were investigated by XPS. No deterioration of the surface stoichiometry occurred after UHPA. On the basis of the C 1s core level shift, SPV on a p-type semiconductor was observed for both Mg-ion-implanted GaN and Mg–N-ion-co-implanted GaN after dehydrogenation annealing subsequent to UHPA. In addition, ARXPS after dehydrogenation showed that the Ga 3d core-level spectrum shifted as the photoelectron take-off angle was varied, which indicated that p-type band bending was generated. Thus, p-type conduction was achieved even in the near-surface region of Mg-ion-implanted GaN with and without N-co-implantation. ARXPS with calibration showed that the surface Fermi level was pinned at 0.5 eV from the conduction band edge after hydrogenation subsequent to UHPA. However, the absence of pinning at E_{CNL} showed that surface disorder was absent after UHPA. SPV was more remarkable for the sample with N-co-implantation. There is a possibility that the density of V_N-related defects was reduced to a greater extend by N-co-implantation combined with UHPA.

Acknowledgments

This work was supported by MEXT "Research and development of next-generation semiconductor to realize energy-saving society" Program Grant Number JPJ005357. Part of this research was also supported by the Polish National Science Centre through Project No. 2018/29/B/ST5/00338. The authors are thankful to Professor T. Hashizume of Hokkaido University, for fruitful discussions.

References

1) D. Ueda, in *Power GaN Devices*, eds. M. Meneghini, G. Meneghesso, and E. Zanoni, (Springer, New York, 2017), Ch. 1.
2) F. Schwierz, Solid-State Electronics **49**, 889 (2005).
3) B. J. Baliga, Semicond. Sci. Technol. **28**, 074011 (2013).
4) S. Kaneki, J. Ohira, S. Toiya, Z. Yatabe, J. T. Asubar, and T. Hashizume, Appl. Phys. Lett. **109**, 162104 (2016).
5) T. Hashizume, S. Kaneki, T. Oyobiki, Y. Ando, S. Sasaki, and K. Nishiguchi, Appl. Phys. Express 11, 124102 (2018).
6) T. Yamada, D. Terashima, M. Nozaki, H. Yamada, T. Takahashi, M. Shimizu, A. Yoshigoe, T. Hosoi. T. Shimura, and H. Watanabe, Jpn. J. Appl. Phys. **58**, SCCD06 (2019).
7) K. Nishiguchi, S. Kaneki, S. Ozaki, and T. Hashizume, Jpn. J. Appl. Phys. **56**, 101001 (2017).
8) T. Kachi, Jpn. J. Appl. Phys. **53**, 100210 (2014).
9) H. Amano et al., J. Phys. D, Appl. Phys. **51**, 163001 (2018).
10) T. Oka, T. Ina, Y. Ueno, and J. Nishi, Appl. Phys. Express **8**, 054101 (2015).
11) D. Ji, A. Agwal, H. Li, W. Li, S. Keller, and S. Chowdhury, IEEE Electron Dev. Lett. **39**, 863 (2018).
12) D. Ji, W. Li, A. Agwal, S. H. Chan, J. Haller, D. Bisi, M. Labrecque, C. Gupta, B. Cruse, R. Lal, S. Keller, U. K. Mishra, and S. Chowdhury, IEEE Electron Dev. Lett. **39**, 1030 (2018).
13) B. N. Feigelson, T. J. Anderson, M. Abraham, J. A. Freitas, J. K. Hite, C. R. Eddy, and F. J. Kub, J. Cryst. Growth **350**, 21 (2012).
14) T. J. Anderson, B. N. Feigelson, F. J. Kub, M. J. Tadjer, K. D. Hobart, M. A. Mastro, J. K. Hite, and C. R. Eddy, Electron. Lett. **50**, 197 (2014).
15) J. D. Greenlee, T. J. Anderson, B. N. Feigelson, K. D. Hobart, and F. J. Kub, Phys. Status Solidi A **212**, 2772 (2015).
16) T. J. Anderson, J. D. Greenlee, B. N. Feigelson, J. K. Hite, K. D. Hobart, and F. J. Kub, IEEE Trans. Semicond. Manuf. **29**, 343 (2016).
17) K. Nomoto, K. Takahashi, T. Oikawa, H. Ogawa, T. Nishimura, T. Mishima, H. G. Xing, and T. Nakamura, ECS Trans. **69**, 105 (2015).
18) T. Oikawa, Y. Saijo, S. Kato, T. Mishima, and T. Nakamura, Nuclear Instruments and Methods in Physics Research B **365**, 168 (2015).

19) T. Narita, T. Kachi, K. Kataoka, and T. Uesugi, Appl. Phys. Exp. **10**, 016501 (2017).
20) T. Niwa, T. Fujii, and T. Oka, Appl. Phys. Express **10**, 091002 (2017).
21) H. Sakurai, M. Omori, S. Yamada, Y. Furukawa, H. Suzuki, T. Narita, K. Kataoka, M. Horita, M. Bockowski, J. Suda, and T. Kachi, Appl. Phys. Lett. **115**, 142104 (2019).
22) M. Akazawa, T. Matsuyama, T. Hashizume, M. Hiroki, S. Yamahata, and N. Shigekawa, Appl. Phys. Lett. **96**, 132104 (2010).
23) T. Narita, D. Kikuta, N. Takahashi, K. Kataoka, Y. Kimoto, T. Uesugi, T. Kachi, and M. Sugimoto, Phys. Status Solidi A 208, 1541 (2011).
24) M. Akazawa, B. Gao, T. Hashizume, M. Hiroki, S. Yamahata, and N. Shigekawa, J. Appl. Phys. **109**, 013703 (2011).
25) M. H. Hecht, Phys. Rev. B **41**, 7918 (1990).
26) J. P. Long and V. M. Bermudez, Phys. Rev. B **66**, 121308 (2002).
27) T. Narita, H. Sakurai, M. Bockowski, K. Kataoka, J. Suda, and T. Kachi, Appl. Phys. Express **12**, 111005 (2019).
28) S. Porowski, I. Grzegory, D. Kolesnikov, W. Lojkowski, V. Jager, W. Jager, V. Bogdanov, T. Suski and S. Krukowski, J. Phys.: Condens. Matter **14**, 11097 (2002).
29) R. Stoklas, D. Gregušová, M. Blaho, K. Fröhlich, J. Novác, M. Matys, Z. Yatabe, P. Kordoš, and T. Hashizume, Semicond. Sci. Technol. **32**, 045018 (2017).
30) M. E. Gulseren, G. Kurt, T. G. U. Ghobadi, A. Ghobadi, G. Salkim, M. Ozturk, B. Butun, and E. Ozbay, Mater. Res. Express **6**, 095052 (2019).
31) D. Briggs and M. P. Seah, *Practical Surface Analysis by Auger and X-ray Photoelectron Spectroscopy* (John Wiley & Sons Ltd., Sussex, 1983), Ch. 9.
32) S. Tanuma, C. J. Powell, and D. R. Penn, Surf. Interface Anal. **17**, 927 (1991).
33) S. Tanuma, C. J. Powell, and D. R. Penn, Surf. Interface Anal. **21**,165 (1993).
34) K. Isobe and M. Akazawa, Jpn. J. Appl. Phys. **59**, 046506 (2020).
35) H. Hasegawa and H. Ohno, J. Vac. Sci. & Technol. B **4**, 1130 (1986).
36) M. Akazawa and H. Hasegawa, Phys. Status Solidi A **195**, 248 (2003).
37) J. L. Lyons and C. G. Van de Walle, NPJ Computational Materials **3**, 12 (2017).
38) C. B. Soh, S. J. Chua, H. F. Lim, D. Z. Chi, W. Liu, and S. Tripathy, J. Phys.: Condens. Matter **16**, 6305 (2004).
39) L. Polenta, A. Castaldini, and A. Cavallini, J. Appl. Phys. **102**, 063702 (2007).
40) T. Tanaka, K. Shiojima, T. Mishima, and Y. Tokuda, Jpn. J. Appl. Phys. **55**, 061101 (2016).

41) I. Boturchuk, L. Scheffler. A. N. Larsen, and B. Julsgaard, Phys. Status Solidi A **215**, 1700516 (2018).

42) K. Iwata, H. Sakurai, S. Arai, T. Nakashima, T. Narita, K. Kataoka, M. Bockowski, M. Nagao, J. Suda, T. Kachi, and N. Ikarashi, J. Appl. Phys. **127**, 105106 (2020).

43) S. C. Choo, L. S. Tan, and K. B. Quek, Solid-St. Electron. **35**, 269 (1992).

44) S. M. Sze and K. K. Ng, Physics of Semiconductor Devices (Wiley, Hoboken, NJ, 2007) 3rd ed., Chap. 3.

45) J.-Y. Duboz, B. Beaumont, J.-L. Reverchon, and A. D. Wieck, J. Appl. Phys. **105**, 114512 (2009).

46) J.-Y. Duboz, M. Laügt, D. Scheck, B. Beaumont, J.-L. Reverchon, A. D. Wieck, and T. Zimmerling, Appl. Phys. Lett. **92**, 263501 (2008).

47) H. Sakurai, M. Omori, S. Yamada, Y. Furukawa, H. Suzuki, T. Narita, K. Kataoka, M. Bockowski, J. Suda, and T. Kachi, Proc. SPIE 10918, Gallium Nitride Materials and Devices XIV, 109180V (2019).

Figure Captions

Fig. 1. (a) Sample preparation sequence. XPS was performed at each process step. (b) Completed sample structure.

Fig. 2. SIMS profiles of [Mg] and [H] in GaN after UHPA for (a) Mg-I/I and (b) Mg–N-I/I.

Fig. 3. AFM images. (a) as-grown GaN (RMS = 0.356 nm). (b) after 1-time SPM treatment (RMS = 0.358 nm). (c) after 10-times-repeated SPM treatment (RMS = 0.390 nm).

Fig. 4. N 1s, Ga LMM Auger, Ga 3d, and N 2s spectra measured at $\theta = 45^{\circ}$ for (a) as-grown, (b) Mg-I/I, (c) UHPA, and (d) dehydrogenation process steps. The intensity is normalized to the area of Ga 3d for each process step. The binding energy is adjusted to be relative to that of Ga 3d spectra.

Fig. 5. Areal ratio $I_{\mathrm{N1s}}/I_{\mathrm{Ga3d}}$ at each process step.

Fig. 6. Schematic diagram illustrating SPV effect.

Fig. 7. C 1s spectra for process steps of (a) as-grown, (b) Mg-I/I, (c) UHPA after Mg-I/I, (d) dehydrogenation after Mg-I/I with subsequent UHPA, (e) UHPA after Mg–N-I/I, and (f) dehydrogenation after Mg–N-I/I with subsequent UHPA. The binding energy was calibrated by setting Au 4f $_{7/2}$ at 84.0 eV prior to this measurement.

Fig. 8. Average values of C 1s core-level shifts over five measurements for each process step.

Fig. 9. Ga 3d and VBM spectra measured for as-grown GaN at $\theta = 45^{\circ}$. The binding energy was calibrated by setting C 1s at 285.0 eV.

Fig. 10. Plots of ($E_{\mathrm{F}} - E_{\mathrm{V}}$) derived from Ga 3d and VBM spectra vs. escape depth for (a) as-grown undoped GaN and (b) as-implanted GaN.

Fig. 11. Ga 3d spectra measured at five θ values for GaN after the final process step of dehydrogenation. The binding energy was calibrated by setting Au 4f $_{7/2}$ at 84.0 eV prior to this measurement. The broken line is guide for the eyes.

Fig. 12. Plots of (E_F – E_V) under X-ray illumination derived from Ga 3d spectra at five θ velues as a function of escape depth for GaN after the final process step of dehydrogenation. (a) Without calibration of SPV effect. (b) With calibration.

Fig. 13. Schematic diagram of charge-up mechanism of surface states. Hatched areas indicate occupied surface states. (a) When E_{FS} locates above E_{CNL}, surface states are ionized negatively. (b) When E_{FS} locates below E_{CNL}, surface states are ionized positively.

Fig. 14. Estimated multiplying factor B as a function of E_{00} for $\Phi = 1\times10^{12}$ cm^{-2} eV^{-1} and $\Phi = 1\times10^{13}$ cm^{-2} eV^{-1}.

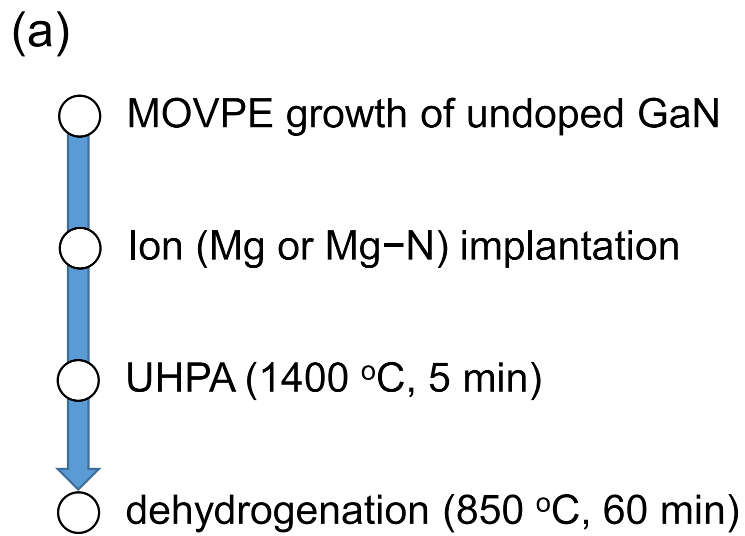

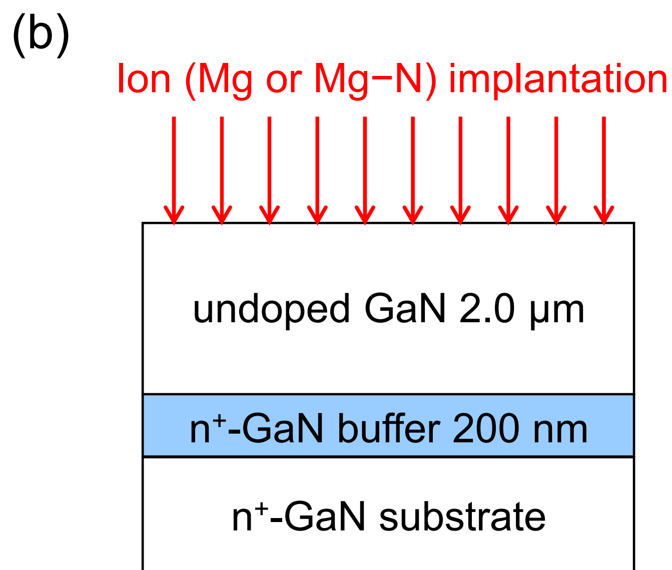

Fig. 1.

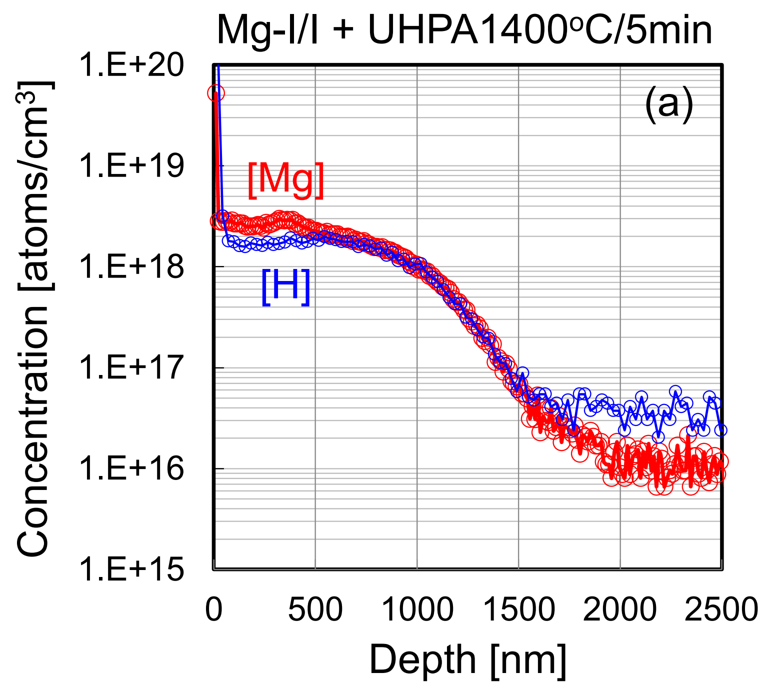

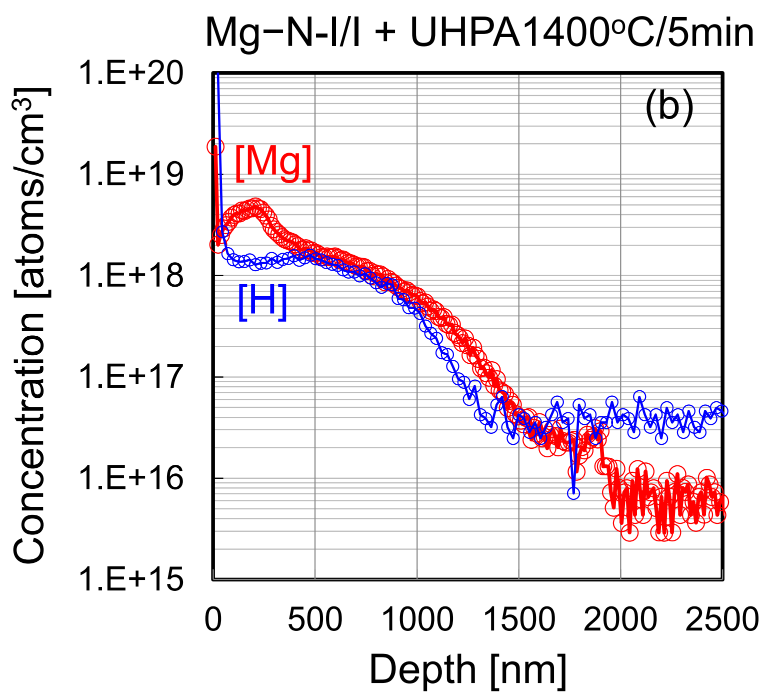

Fig. 2.

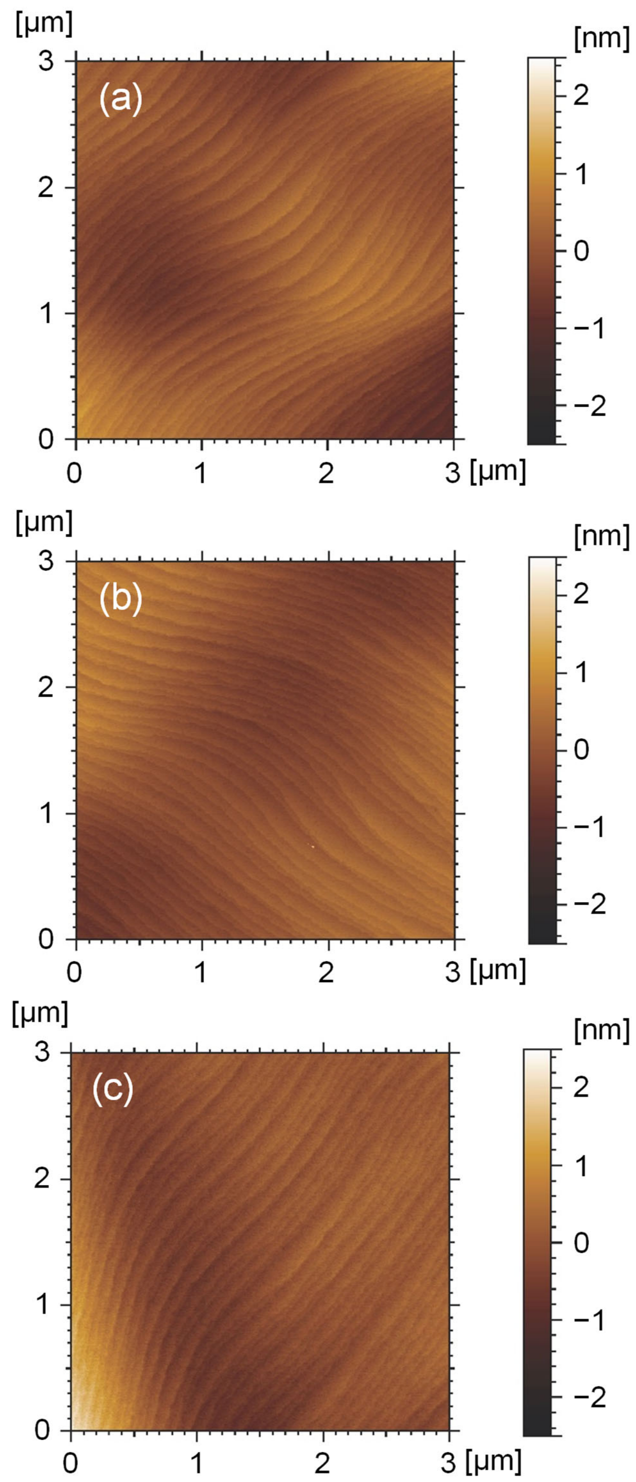

Fig. 3.

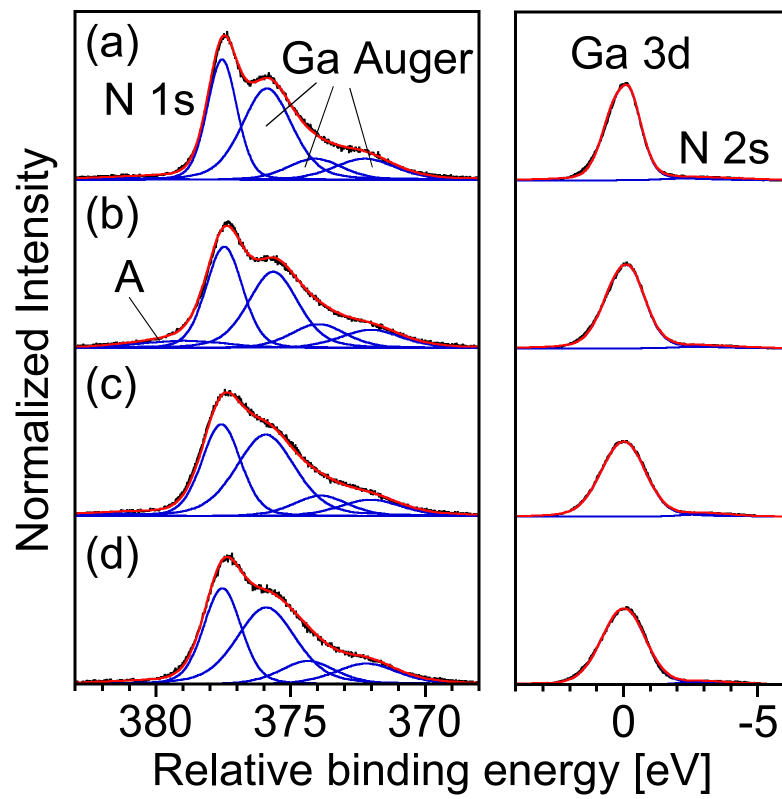

Fig. 4.

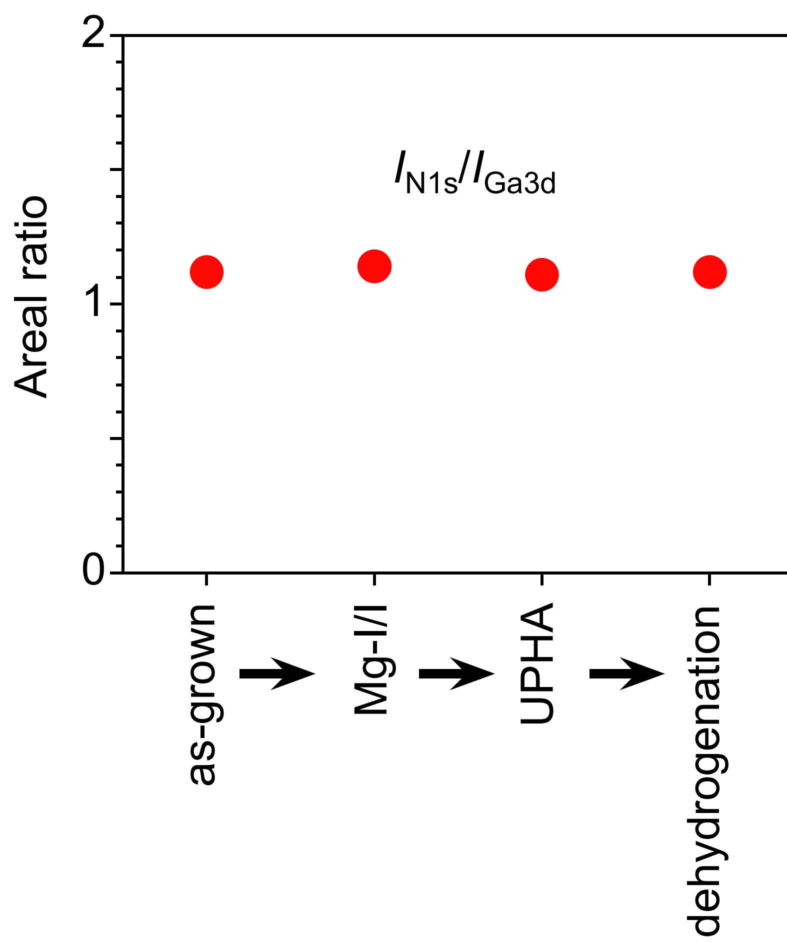

Fig. 5.

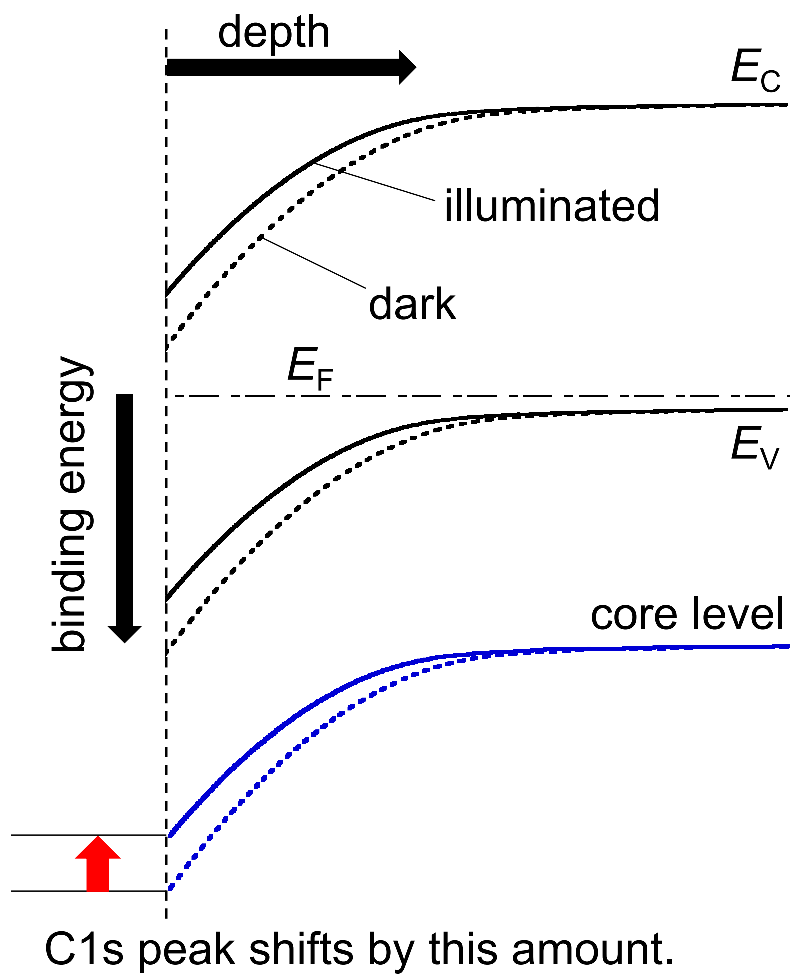

Fig. 6.

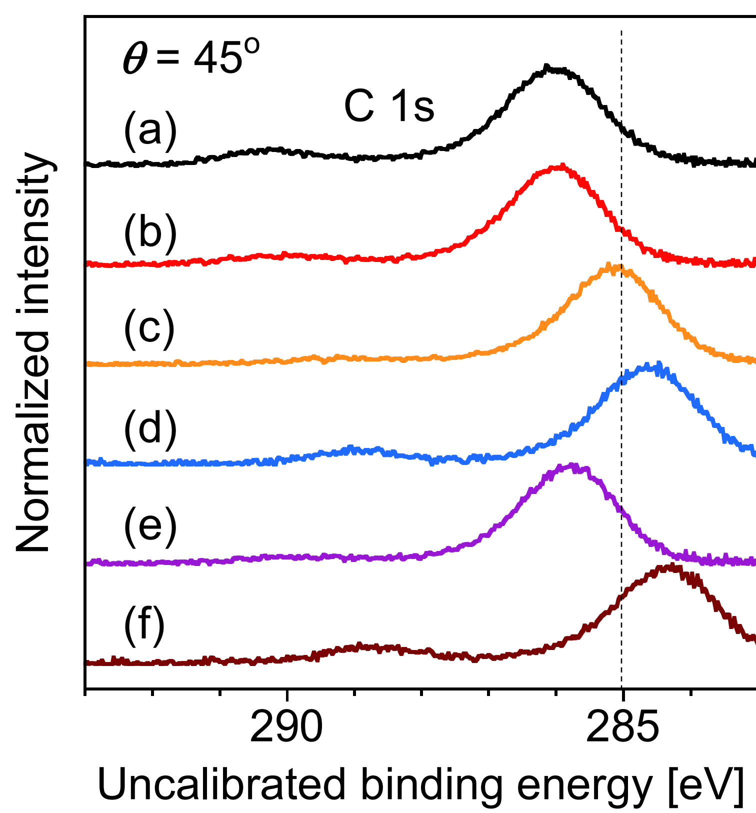

Fig. 7.

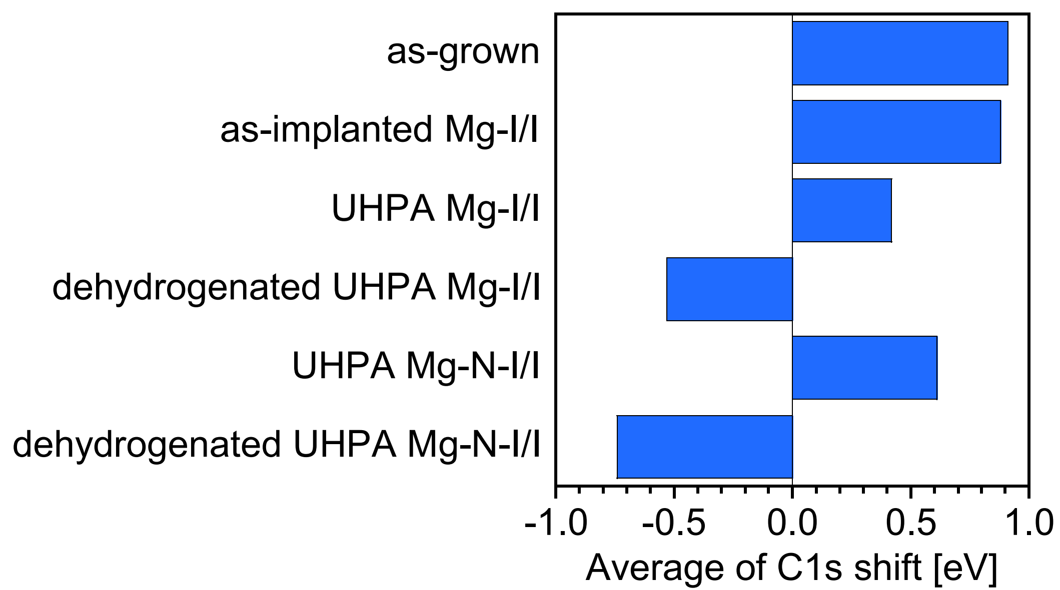

Fig. 8.

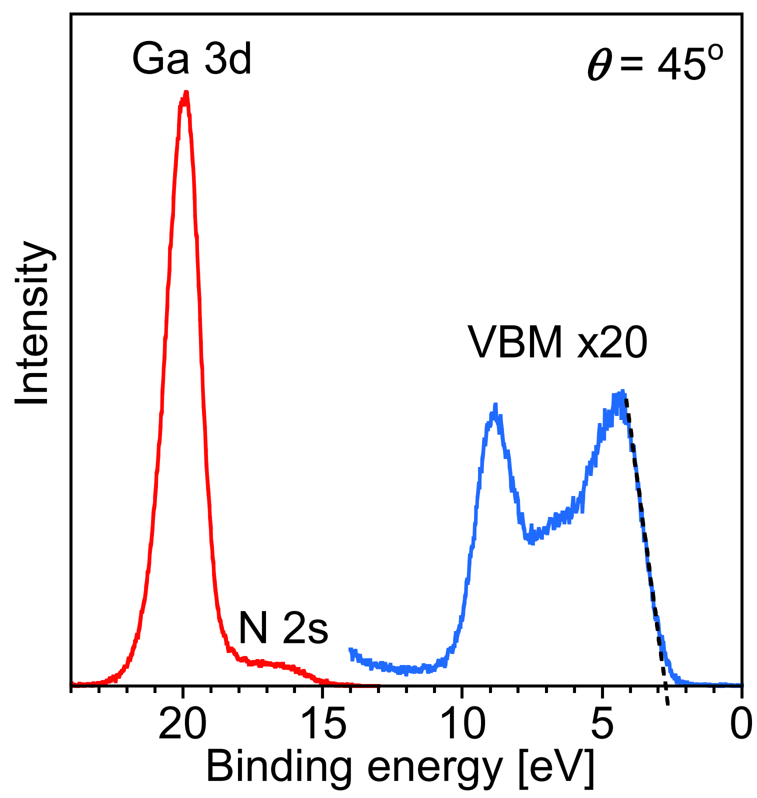

Fig. 9.

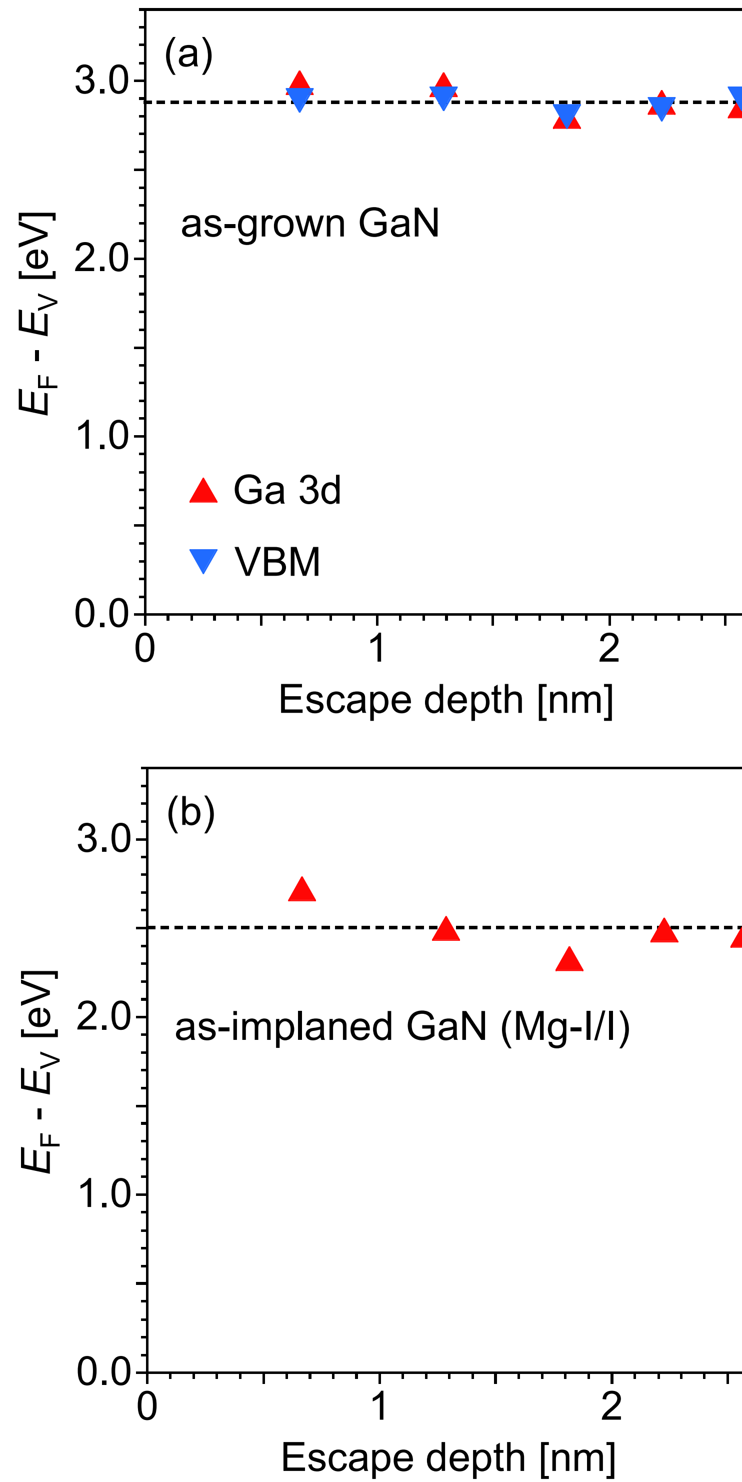

Fig. 10.

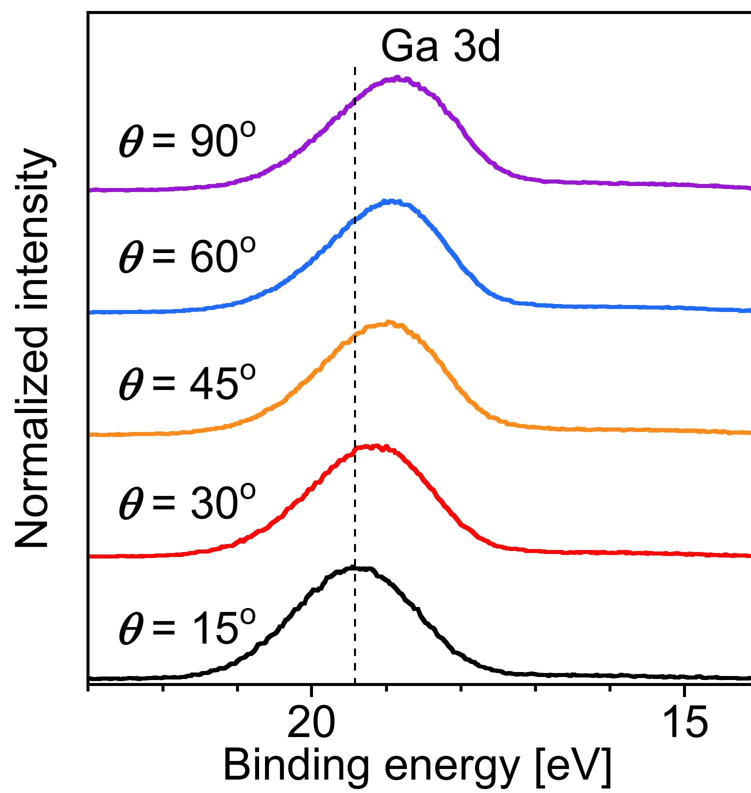

Fig. 11.

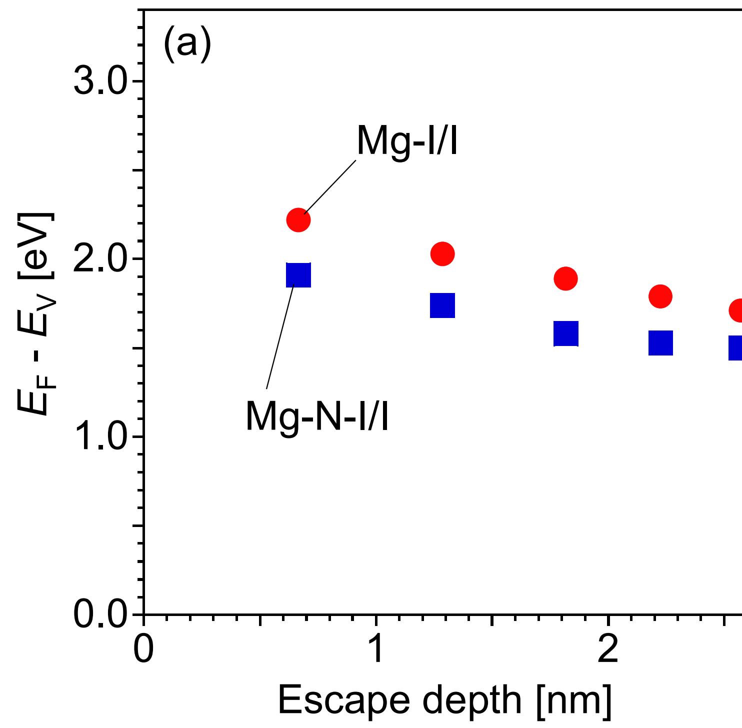

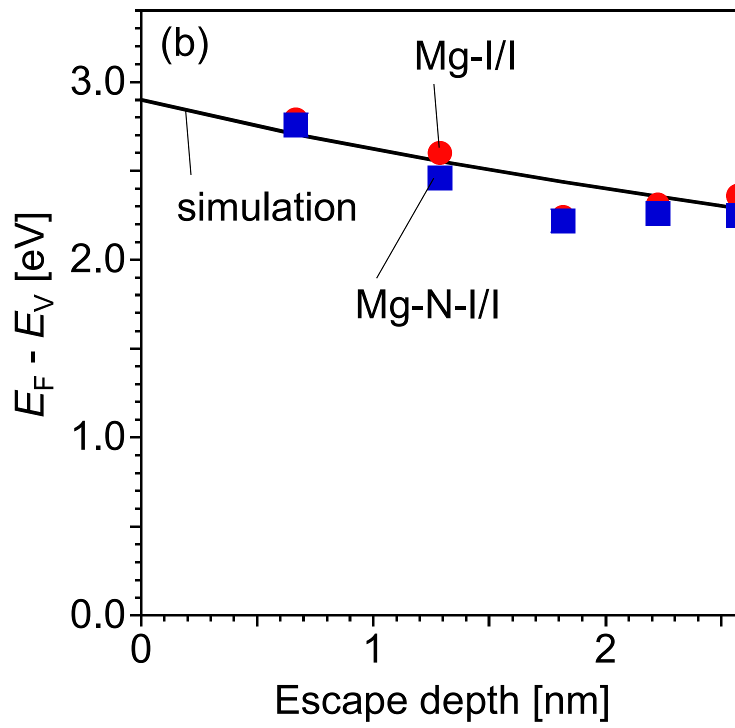

Fig. 12.

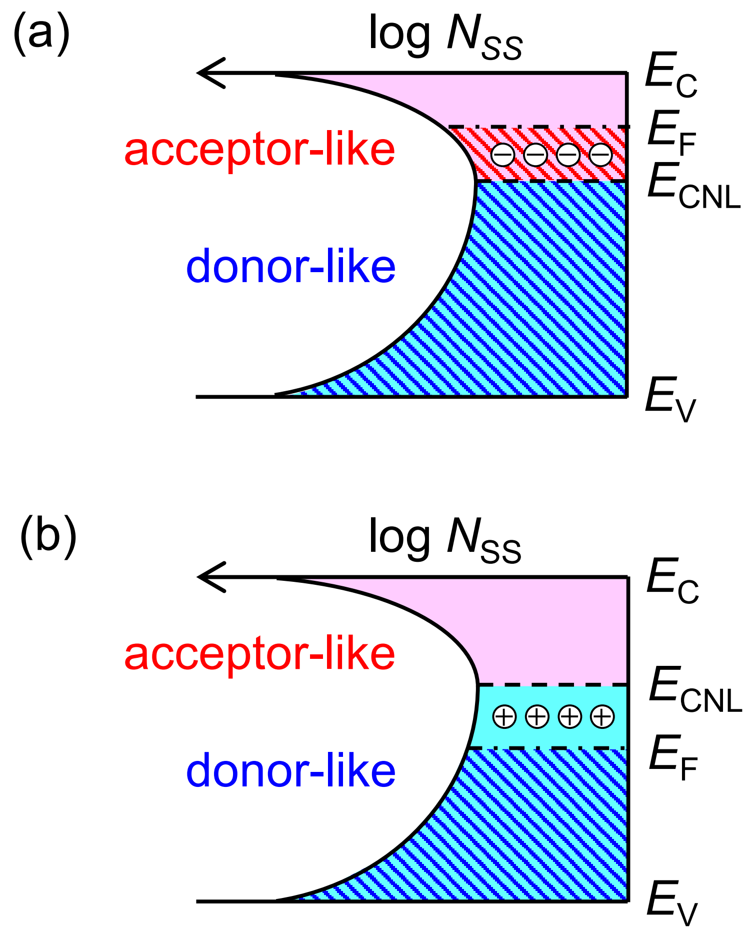

Fig. 13.

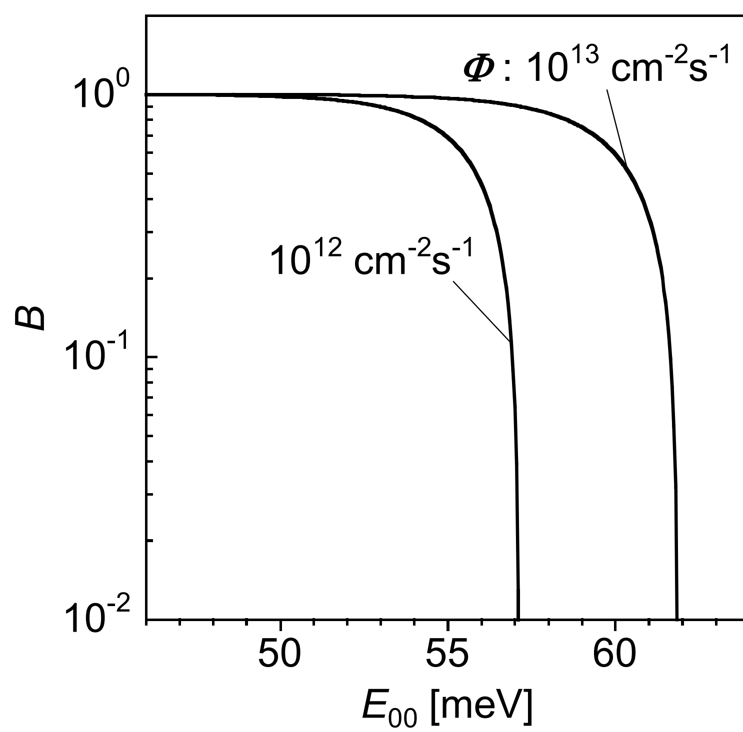

Fig. 14.